Heat and Mass Transfer (2023) 59:2005–2021
https://doi.org/10.1007/s00231-023-03350-2

ORIGINAL ARTICLE

Magneto-convective flows around two differentially heated cylinders

C. Mistrangelo[1] · L. Bühler[1] · H-J. Brinkmann[1] · C. Courtessole[1] · V. Klüber[1] · C. Koehly[1]

Received: 16 June 2022 / Accepted: 13 February 2023 / Published online: 5 June 2023

Abstract
Numerical simulations have been carried out in support of an experimental campaign conducted in the MEKKA laboratory at KIT. The aim is investigating liquid metal heat transfer with an imposed magnetic field in a model geometry relevant for the study of water cooled lead lithium blankets for fusion reactors. In the breeding zone of this blanket concept, cooling pipes are immersed in the liquid metal in which convective motion occurs due to significant temperature gradients. The test-section features a rectangular box containing two horizontal cylinders kept at constant differential temperatures in order to establish a temperature gradient that drives the buoyant flow. A magnetic field **B** is applied parallel to gravity. The magneto-convective flow, which results from the presence of electromagnetic forces and temperature gradients in the fluid, is relatively complex, since the liquid metal has to move around the cylinders. For weak magnetic fields, a convective recirculation is fed by a jet-like flow formed by the boundary layers that detach from the pipe walls and recombine behind the obstacles. For sufficiently strong **B**, the thermal field resembles that of a conductive regime with vertical isotherms and the fluid is nearly stagnant in most of the cavity except in layers parallel to magnetic field lines and tangent to the cylinders. The rate of convective heat transfer decreases with an increase of the magnetic field. Numerical simulations complement experimental results and give insight into phenomena that cannot be directly analyzed by means of measured quantities.

1 Introduction

In the frame of the European fusion research program coordinated by EUROfusion, the European Consortium for Development of Fusion Energy, liquid metal blanket concepts are developed, which will be experimentally tested in the International Thermonuclear Experimental Reactor (ITER). The latter represents the key experimental phase required to pass from the presently available research devices to a future DEMOnstration nuclear fusion power plant [1]. In these systems, the fusion reaction takes place in a very hot plasma, an ionized gas of two hydrogen isotopes deuterium D and tritium T, which is confined by a strong magnetic field to a toroidal geometry.

In the blanket, which is the structure that surrounds the fusion plasma, fast neutrons generated from the D-T fusion reaction are absorbed by a lithium-containing liquid metal alloy, breeding the fuel component tritium and releasing their kinetic energy in form of volumetric heating. In the water-cooled lead lithium (WCLL) blanket concept, currently under investigation in the EUROfusion research activities [2], the heat is removed by a large number of cooling tubes immersed in the liquid metal flowing in the breeding units. The design of the WCLL test blanket module for ITER is shown in Fig. 1. The latter consists of modules stacked along the poloidal direction and fixed to a common back supporting structure housing the liquid metal feeding pipes. Liquid lead lithium, PbLi, serves as tritium breeder, neutron multiplier and heat carrier.

Since the liquid metal is electrically conducting, pressure driven or buoyant flows interact with the strong plasma-confining magnetic field leading to the occurrence of induced electric currents and intense electromagnetic Lorentz forces, which affect pressure drop, flow distribution and heat transfer in the blanket. Such interaction between flow and magnetic field, so-called magnetohydrodynamics (MHD), has been attracting considerable attention in many areas of applied science.

✉ C. Mistrangelo
chiara.mistrangelo@kit.edu

[1] Karlsruhe Institute of Technology (KIT), P.O. Box 3640, 76021 Karlsruhe, Germany

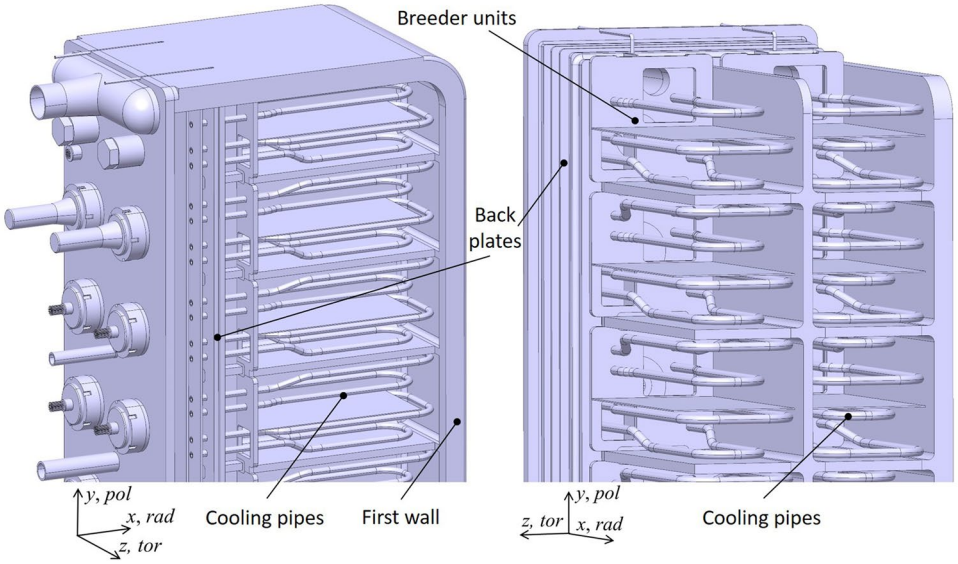

Fig. 1 Design of a WCLL test blanket module for ITER; view on the cooling pipes in the breeding zones. The so-called first wall faces the fusion plasma

As a result of the design of the WCLL blanket cooling system, the liquid metal has to flow around cooling pipes following complex paths. Since the forced flow is relatively small and temperature gradients are large, it is expected that buoyancy dominates and determines the flow pattern as a result of a balance with electromagnetic Lorentz forces. The arrangement of cooling tubes plays a critical role to assess the blanket feasibility, since it has to ensure an efficient heat power removal from the liquid metal, avoiding the occurrence of local hot spots in the thermal field. The present paper sheds some light on magneto-convective heat transfer around obstacles, such as the cooling pipes, and helps gaining insight in major flow phenomena, by predicting 3D circuits of electric currents and flow patterns.

Besides interest in fusion engineering, heat transfer in liquid metals exposed to a strong magnetic field constitutes a fundamental problem in magnetohydrodynamics. There exists a number of publications on forced and mixed convection in pipe and duct flows exposed to a magnetic field, e.g. [3–6], and on free or mixed convection in cylindrical or rectangular cavities [7–11]. A comprehensive list of references can be found in a recent review paper by Zikanov et al. [12]. Thermal convection with an imposed magnetic field is of great importance also in industrial applications such as metallurgy [13] or crystal growth of semiconductors [14, 15]. On the other hand, MHD heat transfer at immersed bodies, such as water-cooled pipes, has not attracted similar attention. Some studies have been carried out to investigate the influence of a heat-conducting solid obstruction in the shape of a baffle or a block on natural convection in an enclosure without magnetic field [16, 17]. In [18] two dimensional laminar free convection with a horizontal magnetic field in a cavity containing a square insulated block was studied. The side walls of the enclosure were insulated, and top and bottom walls differentially heated. Results showed that the presence of an insulated block contributes to the enhancement of the heat transfer rate depending on the block size and the strength of the magnetic field. Few publications are available for fully established buoyant MHD flow in long vertical [19] or horizontal [20] ducts in which a single coaxial fluid-internal cylindrical obstacle is present. While buoyant flows in quite complex geometries, such as entire breeder units of a fusion blanket, have been studied for special cases [21, 22], a systematic investigation of MHD heat transfer at individual pipes is still missing.

Therefore, the present work aims at investigating MHD phenomena and related buoyant heat transfer at fluid-internal cylindrical obstacles for various strengths of the magnetic field and applied temperature differences. The flow in a geometry featuring a box containing two parallel differentially heated horizontal cylinders is analyzed by 2D and 3D numerical simulations and the heat transfer rate is quantified in terms of the non-dimensional Nusselt number. Results are verified by comparison with experimental data.

2 Definition of the problem

For systematic investigation of liquid metal heat transfer in strong magnetic fields, a generic model problem has been defined as shown in Fig. 2. Here, the geometry with coordinate system and dimensions is displayed, as used for the numerical study. A magnetic field **B** is imposed in y -direction opposite to gravity. Walls perpendicular to the applied magnetic field and colored in blue are called Hartmann walls, while those parallel to **B** at $z = \pm 100$ mm are named side walls. The walls at $x = \pm 100$ mm are referred

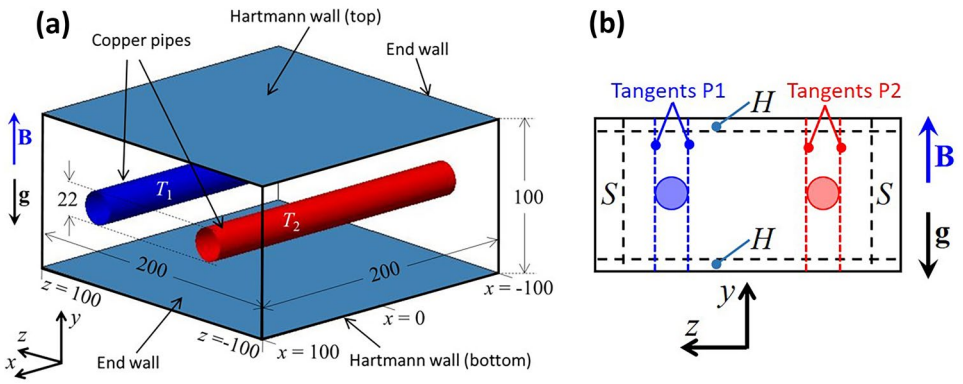

Fig. 2 **a** Geometry used for simulations of 3D magneto-convective flow. Dimensions are given in mm. **b** Side layers (*S*) and Hartmann layers (*H*) are schematically indicated together with internal layers tangent to the pipe walls (P1 and P2). Parallel layers form also along the end-walls

to as end-walls. Two differentially heated isothermal pipes aligned with the x - direction penetrate the end-walls and have an external diameter of 22 mm. It is known that the presence of an applied uniform magnetic field gives rise to induced electrical currents and Lorentz forces that extend flow structures along **B** direction [23], where the flow becomes invariant if the imposed magnetic field is sufficiently strong. Significant velocity gradients remain in regions close to walls perpendicular to the magnetic field, called Hartmann layers (*H*), where viscous forces still play an important role. Gradients of flow variables occur also in the **B**-parallel side layers (*S*) that form both along side and end-walls, and in a zone around the tangents to the pipe walls (P1 and P2), as displayed schematically in Fig. 2b.

The selected geometrical configuration corresponds to the one used in an experimental campaign carried out in the liquid metal laboratory MEKKA at KIT in which the eutectic liquid metal alloy GaInSn is used as model fluid. A detailed description of the test-section can be found in [24].

Figure 3 shows an isometric view of the design of the experiment. It consists of a leak-tight rectangular box made

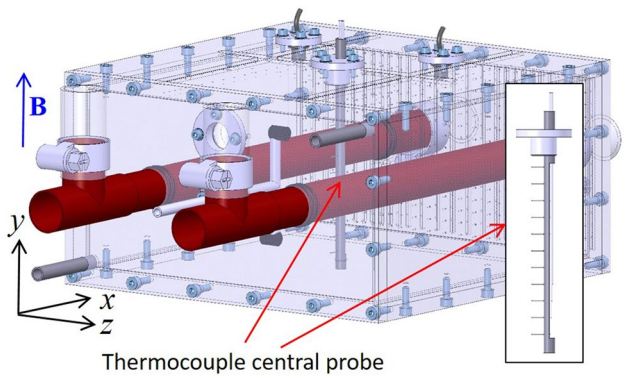

Fig. 3 Design of the experimental test-section. The rectangular box contains two parallel differentially heated pipes and it is equipped with a large number of thermocouples. In the center of the box a temperature probe is inserted, which is shown in the subplot on the right. It consists of 11 equidistantly distributed thermocouples type T (Cu-CuNi), fixed and sealed with a flange on the top of the box

of electrically insulating PEEK. Two parallel copper pipes are inserted in the container. The outer surface of the pipes has been coated with a 2 μm thin silicon carbide layer, which ensures a good thermal conductivity and provides sufficient protection against corrosion attack. It also prohibits induced currents from closing into the pipes, avoiding thermoelectric effects between pipe walls and liquid metal. A temperature gradient that drives the buoyant flow is realized in the experiments by setting a temperature difference between the two copper pipes immersed in the liquid metal. One tube is heated, while the other pipe is cooled to serve as heat sink. The pipes are maintained at constant temperatures $T_1 < T_2$ during the experiments. The described set-up permits establishing well defined boundary conditions, as required when performing numerical calculations that will be compared with experimental data.

The dimensions of the box, $200 \times 100 \times 200$ mm^3 (see Fig. 2), are such that, after applying thermal insulation on all external walls, the test-section fits in the gap of the large dipole magnet available in the MEKKA laboratory [25]. The magnetic field is quite uniform, with deviations smaller than 1% within a region of $800 \times 168 \times 480$ mm^3. The maximum strength of the magnetic field is 2.1T.

During the experiments temperature is recorded on the walls of the container and inside the fluid. The temperature distribution in the box has been carefully monitored in order to define the thermo-physical properties of the fluid, and a very precise data acquisition system has been used to record temperatures and to quantify the heat transfer. All temperatures are measured with respect to a 75-channel ice-point reference system (Kaye K170) accurate to 0.02 °C. Thermoelectric voltages are recorded with a resolution of 1 μV (Beckhoff KL3312) ensuring that the temperatures are measured with an accuracy of 0.05 °C on all the channels. Figure 4 shows the four lines along which the temperature has been recorded and compared with numerical simulations. Data has been taken along the vertical y - direction in the middle of the test-section at $z = 0$, both on the end-wall at $x = 100$ mm (EW2) and at $x = x_P = -6.5$ mm where the tips of the thermocouples on the central probe rod (CP) are

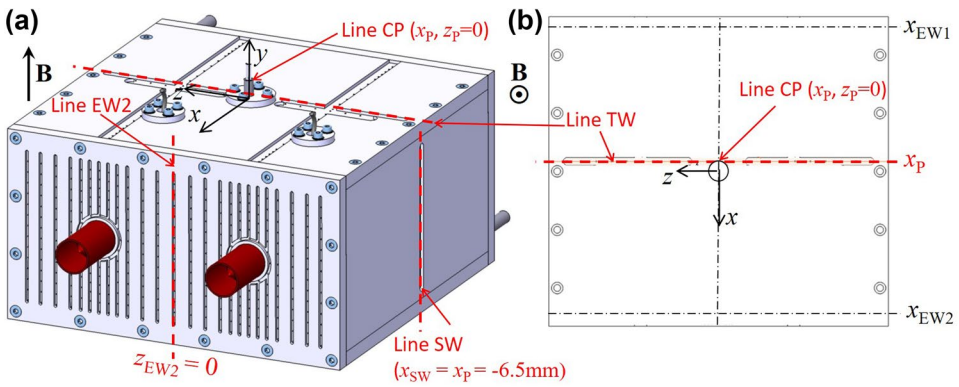

Fig. 4 Design of the experimental test-section. Positions of thermocouples on an end-wall (EW2), on the Hartmann top wall (TW), on a side wall (SW), and along the central probe (CP)

positioned. Temperature has been recorded also at $x = x_P$ on a side wall (SW) along y and on the top wall (TW) of the test-section along the z - direction.

The experimental procedure consists in setting a constant temperature difference between the pipes and recording all temperature signals, once the thermal steady state is reached, for different values of the applied magnetic field. A detailed description of the experimental procedure and results is published in a companion paper [26].

3 Governing equations and characteristic parameters

We analyze liquid metal flows exposed to an externally applied uniform magnetic field $\mathbf{B} = B\hat{\mathbf{y}}$ (see Fig. 2). The flow is driven by buoyancy forces due to temperature variations between heated and cooled pipes. The viscous incompressible flow is described by equations for balance of momentum, conservation of mass, and currents are calculated by means of Ohm's law

$$\rho_0\Big(\frac{\partial}{\partial t} + \mathbf{v}\cdot\nabla\Big)\mathbf{v} = -\nabla p + \rho_0\nu\nabla^2\mathbf{v} - \rho_0\beta(T - T_0)\mathbf{g} + \mathbf{j}\times\mathbf{B}, \tag{1}$$

$$\nabla\cdot\mathbf{v} = 0, \quad \mathbf{j} = \sigma(-\nabla\phi + \mathbf{v}\times\mathbf{B}). \tag{2}$$

Here $\mathbf{v}$, $\mathbf{j}$, $\mathbf{B}$ and ϕ denote velocity, current density, applied magnetic field, and electric potential. In Eq. (1) p is the deviation of pressure from isothermal hydrostatic conditions at the reference temperature $T_0 = (T_2 + T_1)/2$ and $\mathbf{g} = -g\hat{\mathbf{y}}$ stands for the gravitational acceleration. It is assumed and verified during the analysis that the magnetic Reynolds number, expressing the ratio of advection to diffusion of magnetic field, is very small, $Re_m = \mu\sigma u_0 L \ll 1$, where u_0 is a typical velocity and L a characteristic size of the problem. This implies that the flow-induced magnetic field can be neglected compared to the externally imposed magnetic field and the latter remains undisturbed by the flow. The physical properties of the fluid, such as the reference density ρ_0, the kinematic viscosity ν, the volumetric thermal expansion coefficient β, the electric conductivity σ and the magnetic permeability μ, are considered constant and taken from reference [27]. Density changes due to temperature variations in the liquid metal, which give rise to convective motions, are described by the Boussinesq approximation in the buoyancy term in Eq. (1) so that $\rho = \rho_0\big[1 - \beta(T - T_0)\big]$.

The electric potential ϕ is determined by a Poisson equation obtained by combining Ohm's law (2) and the condition for charge conservation $\nabla\cdot\mathbf{j} = 0$:

$$\nabla^2\phi = \nabla\cdot(\mathbf{v}\times\mathbf{B}). \tag{3}$$

The distribution of temperature T in the fluid is given by the energy balance equation

$$\rho_0 c_p\Big(\frac{\partial T}{\partial t} + (\mathbf{v}\cdot\nabla)T\Big) - k\nabla^2 T = 0, \tag{4}$$

where c_p is the specific heat of the fluid at constant pressure and k the thermal conductivity.

As kinematic boundary condition at the walls the no-slip condition, $\mathbf{v} = 0$, is applied. All walls including the ones of the pipes, which are covered by a ceramic coating, are electrically insulating, $\partial\phi_w/\partial n = 0$, the ones of the rectangular box are adiabatic, $\partial T/\partial n = 0$, while the pipes are kept at constant differential temperatures T_1 and T_2. These boundary conditions have been chosen according to the set-up of the experiments performed in the MEKKA laboratory at KIT (see Section 2).

The flow is characterized by two dimensionless numbers that describe the ratios of forces acting on the flowing liquid metal. The non-dimensional parameters are the Hartmann number, Ha and the Grashof number, Gr:

$$Ha = BL\sqrt{\frac{\sigma}{\rho_0\nu}}, \quad Gr = \frac{g\beta\Delta T L^3}{\nu^2}. \tag{5}$$

The former one gives a non-dimensional measure for the strength B of the imposed magnetic field and its square

quantifies the relative importance of electromagnetic and viscous forces. The Grashof number represents the ratio of buoyancy to viscous forces and it is proportional to a typical temperature difference ΔT, which is defined in the present problem as half of the temperature difference between the pipes, $\Delta T = \left(T_2 - T_1\right)/2$. The quantity L, known as Hartmann length, is taken as half of the dimension of the test-section measured along magnetic field direction, i.e. $L = 50$ mm. For the magneto-convective flow under investigation, a velocity scale $u_0 = \rho_0 g \beta \Delta T / \sigma B^2$ can be obtained as a result of a balance between buoyant and electromagnetic forces. With this definition the Reynolds number $Re = u_0 L/\nu$, which expresses the ratio between inertial and viscous forces, is equivalent to Gr/Ha^2.

The liquid metal used for the experiments has a low Prandtl number, $Pr = \nu \rho c_p / k = 0.029$. It means that thermal diffusion dominates over the viscous momentum transport.

The heat transfer in the established convective flow is quantified in terms of the Nusselt number

$$Nu = \frac{hL}{k}, \tag{6}$$

where the heat transfer coefficient h determines the average heat flux at the surfaces of the pipes, i.e. $\overline{q} = h \Delta T$. Since $\overline{q}$ and ΔT are known from simulations or experiments, the determination of h and Nu is straightforward.

4 Numerical results

4.1 Numerical procedure

Equations (1)-(4) have been implemented in the open source code OpenFOAM. A cell-centered (collocated) finite volume method is used to discretize the equations. A segregated solver is employed and for the coupling between pressure and velocity the Pressure-Implicit with Splitting of Operators (PISO) algorithm available in OpenFOAM is used. The solution of pressure and velocity equations is obtained by using preconditioned conjugate and bi-conjugate gradient solvers, respectively. The Poisson equation for the electric potential is solved with an algebraic multigrid method. The Lorentz force is treated explicitly and defined at cell-centers. Required centroid currents are obtained by interpolation from the face current fluxes in divergence form by using the vector identity $\mathbf{j} = \nabla \cdot (\mathbf{jr})$, where $\mathbf{r}$ is the distance vector [28, 29], in order to avoid spurious contributions to the Lorentz force introduced by discretisation errors. This current conservative interpolation procedure is crucial for accurate numerical predictions of MHD flows under strong magnetic fields. For discretisation of convective terms, the standard Gaussian finite volume integration is employed, together with a second order skewness-corrected interpolation scheme required when using non-orthogonal meshes, as considered in the present work.

Accurate simulations of MHD flows require a proper resolution of the thin boundary layers that form along all walls and of internal layers that develop along magnetic field lines caused by the presence of geometrical or electrical discontinuities. In the problem under investigation internal layers form tangent to the pipes and parallel to the magnetic field (see Fig. 2b). We can distinguish between two types of wall shear layers: the Hartmann layers, which occur at walls where $\mathbf{B}$ has a perpendicular component, and the side layers (or parallel layers), which emerge at walls parallel to the magnetic field. The thickness of these layers reduces by increasing the intensity of the magnetic field and can be expressed in terms of the Hartmann number Ha (5). The typical thickness of the Hartmann layers is of $O(Ha^{-1})$, while that of side layers scales as $O(Ha^{-1/2})$. Analysis of fully developed MHD flows in square channels showed that, in order to predict accurately velocity distribution and pressure gradient in a duct, at least 7 points are necessary in the Hartmann layers and 20 nodes in the side layers [30]. For the present simulations two topologically different meshes have been used. For small and moderate Hartmann numbers, a structured grid has been employed with points clustered near the walls and around the lines tangent to the pipes and aligned with $\mathbf{B}$ in order to resolve boundary and internal layers. With the purpose of reducing the total number of computational cells for simulations of flows under intense magnetic fields and to optimize the mesh size for 3D calculations, a hybrid grid with local refinement has been generated, characterized by geometry-aligned prism layers near the walls of box and pipes, a regular core mesh and an unstructured region to join the different grid portions. Three dimensional simulations needed up to $6 \cdot 10^6$ cells in the geometry and have been performed on the supercomputers JFRS - 1 at IFERC - CSC and on Marconi - CINECA by using 240 CPUs.

Numerical simulations have been performed to predict the MHD convective flow in the test-section described in Section 2 and to compare the results with measured quantities. In the following, for a given magnetic field $\mathbf{B}$ and a defined temperature difference ΔT, transient numerical simulations are performed until steady state solutions are obtained or until time-dependent solutions reach converged statistics. Then, the heat transfer in the model geometry is analyzed in terms of the Nusselt number. First, we discuss results obtained by 2D simulations, namely by assuming that the rectangular box is infinitely long in x - direction and the end-walls do not affect the flow. We assume that fully developed thermal and hydraulic conditions are reached at sufficient distance from the end-walls. In a successive step, we perform 3D calculations considering the real axial size of the test-section and we investigate the closing path of the

induced axial currents and the distribution of the electric potential at the parallel end-walls at $x = \pm 100$ mm (see Fig. 2).

4.2 Fully developed flow

In this section, we analyze fully developed MHD buoyant flows, like the one expected, at least in a certain range of parameters, at some distance from the end-walls and in particular on the symmetry plane $x = 0$. A parametric study has been carried out to investigate the influence of the magnetic field strength and the applied temperature difference between the pipes on flow distribution and heat transfer in the model geometry. Because of the assumption of fully established thermal and hydraulic conditions along x, i.e. $\partial/\partial x = 0$, the electric potential becomes constant and equal to the reference potential $\phi_{ref} = 0$. When there are no potential differences in the fluid, results do not depend on the wall conductance, since potential differences are already equalized in the fluid and there will be no currents exchanged with the walls, independent of their conductivity. Therefore, 2D results shown in the following apply for any wall conductivity at sufficient distance from the end-walls.

In Fig. 5 contours of temperature (top), velocity magnitude (middle) and axial current density (bottom) are plotted for axially fully developed magneto-convective flows at $Gr = 2.5 \cdot 10^7$, i.e. for a temperature difference $\Delta T = 17.34$ K, and for four Hartmann numbers. For $Ha < 40$ ($B < 0.015$ T) time-dependent flow patterns appear triggered by the increased buoyancy effects. The unstable flow is characterized by a large-scale recirculation formed by the fluid that moves upwards in the boundary layers around the warm pipe. The layers detach from the tube and merge again at some distance behind the cylinder while flowing towards the upper wall of the box. The ascending thermal plume impinges against the cavity top wall and turns downwards, flowing towards the low-temperature pipe. The cold boundary layer flow detaches from the cylinder and recombines to feed the region near the bottom of the container. An example of time-dependent flow is shown in Fig. 6, where instantaneous contours of velocity magnitude (a), temperature (b), vorticity in logarithmic color scale (c) and axial current density (d) are displayed for axially developed magneto-convective flow at $Gr = 2.5 \cdot 10^7$ and $Ha = 25$.

For the flow at $Ha = 50$, shown in Fig. 5, small deviations between instantaneous and time-averaged variable values are observable and the temperature field is stratified so that isotherms are almost horizontal. The flow pattern is similar to the one described above for the unstable flow with a large convective motion sustained by the detached boundary layers that form around the pipes. By further increasing the Hartmann number, the flow becomes stationary and temperature contours tilt progressively such that isotherms tend to become vertical, as in a pure conduction case, since convection is damped by more intense Lorentz forces. The velocity distribution becomes regular and well organized.

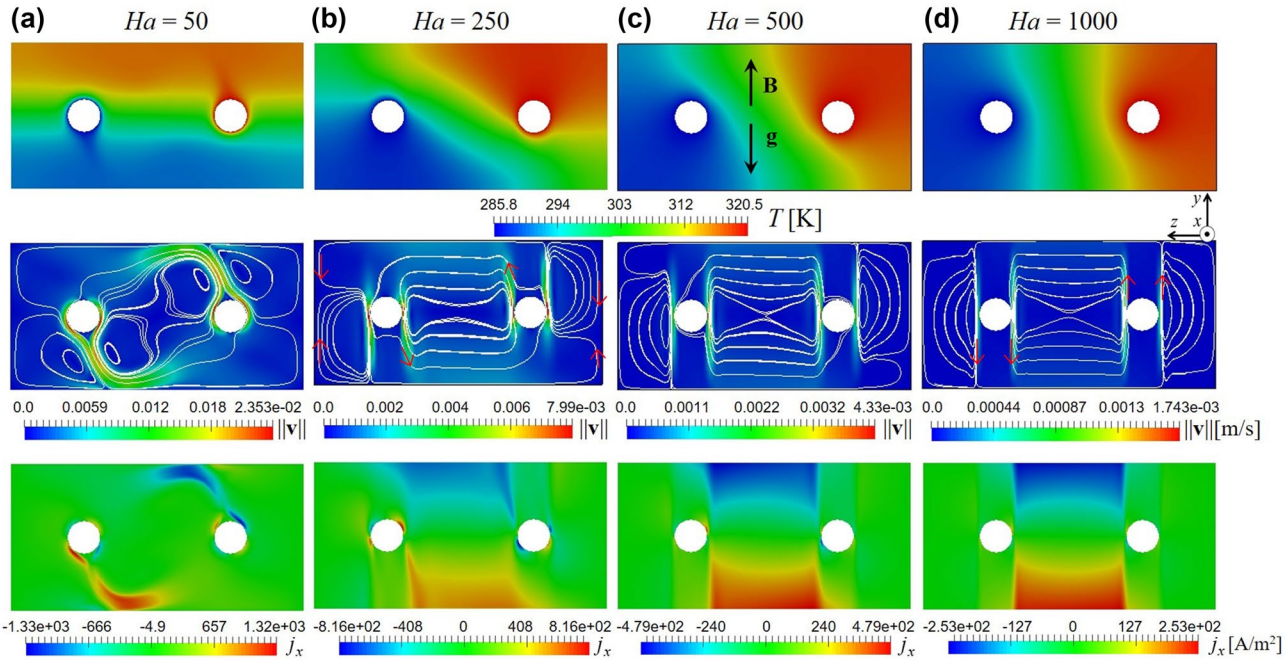

Fig. 5 Axially fully developed MHD convective flow at $Gr = 2.5 \cdot 10^7$ ($\Delta T = 17.34$ K) and four Hartmann numbers, $Ha = 50$ (**a**), 250 (**b**), 500 (**c**), 1000 (**d**). Contours of temperature (top), velocity magnitude (middle) and axial current density (bottom) are plotted. White lines are velocity streamlines

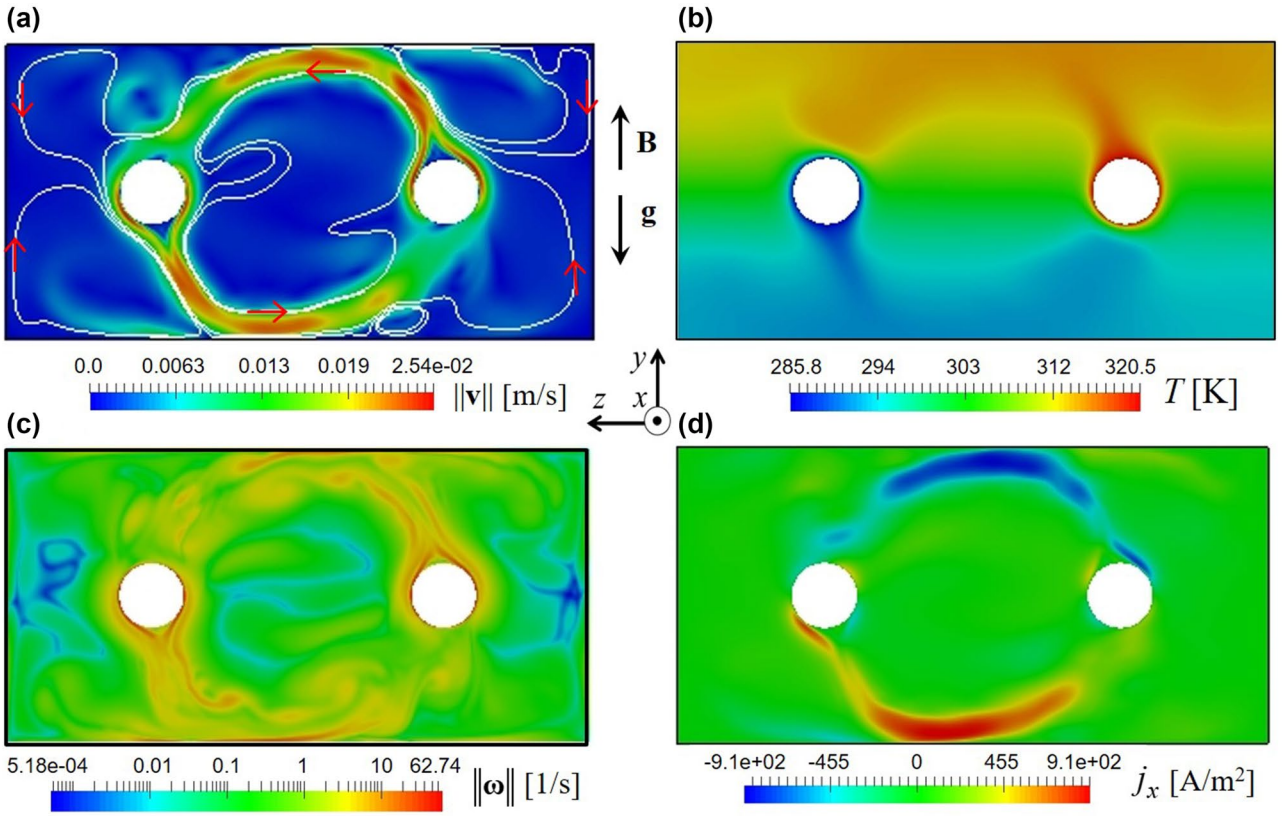

Fig. 6 Instantaneous contours of velocity magnitude (**a**), temperature (**b**), vorticity in logarithmic color scale (**c**) and axial current density (**d**) are displayed for the axially fully developed magneto-convective flow at $Gr = 2.5 \cdot 10^7$ and $Ha = 25$. White paths in (**a**) are velocity streamlines

The flow is characterized by two convective cells located between side walls and pipes and a central, almost square, convective cell between the tubes. The highest velocities are found in internal layers tangent to the pipe walls and aligned with the magnetic field direction. By rising the magnetic field, while keeping ΔT constant, temperature and velocity distributions become more symmetric with respect to the vertical mid-plane $z = 0$, the maximum velocity magnitude decreases and the thickness of the layers becomes smaller (see Fig. 5 (middle)). This is due to the fact that the intensity of braking electromagnetic forces becomes much larger than the buoyant forces. For large Ha the convective motion weakens and in the region between tubes and side walls at $z = \pm 100$ mm the motion is strongly damped. For the flow at $Ha = 50$ depicted in Fig. 5a, the maximum velocity is 23.5 mm/s, while at $Ha = 1000$ the maximum velocity is only about 1.74 mm/s.

In these 2D simulations, it is assumed that the rectangular box is long enough for the flow to reach fully developed thermal and hydraulic conditions, so that no axial electric potential difference builds up and electric currents induced in the liquid metal only flow in axial direction. Contours of axial current density $j_x = -u_z B$, which is induced by the interaction between the applied magnetic field and the transverse velocity component u_z, are depicted in Fig. 5 on the bottom.

In Fig. 7, temperature and velocity fields are shown for the flows at a smaller Grashof number, $Gr = 5 \cdot 10^6$ ($\Delta T = 3.475$ K), and four Hartmann numbers. The comparison of these contours with those depicted in Fig. 5 for the flows at $Gr = 2.5 \cdot 10^7$ shows that, when the temperature difference is smaller, a vertical orientation of the isotherms is reached already when a weaker magnetic field is applied (cf. Figs. 7d and 5d, which have a similar temperature distribution).

The intensity of the convective heat transfer can be quantified by the dimensionless Nusselt number Nu, defined in Eq. (6). Its variation as a function of the Grashof number Gr is shown in Fig. 8 for different Hartmann numbers Ha. The Nusselt number is normalized by the one obtained for the flow at $Gr = 0$ in which the heat is transferred exclusively by conduction. It should be noted that, with the definition of the Nusselt number according to Eq. (6), $Nu(Gr = 0) = Nu_0 \neq 1$. A comparison of the curves given for various Ha indicates that stronger electromagnetic forces, which are induced when the intensity of the magnetic field becomes larger, reduce the heat transfer.

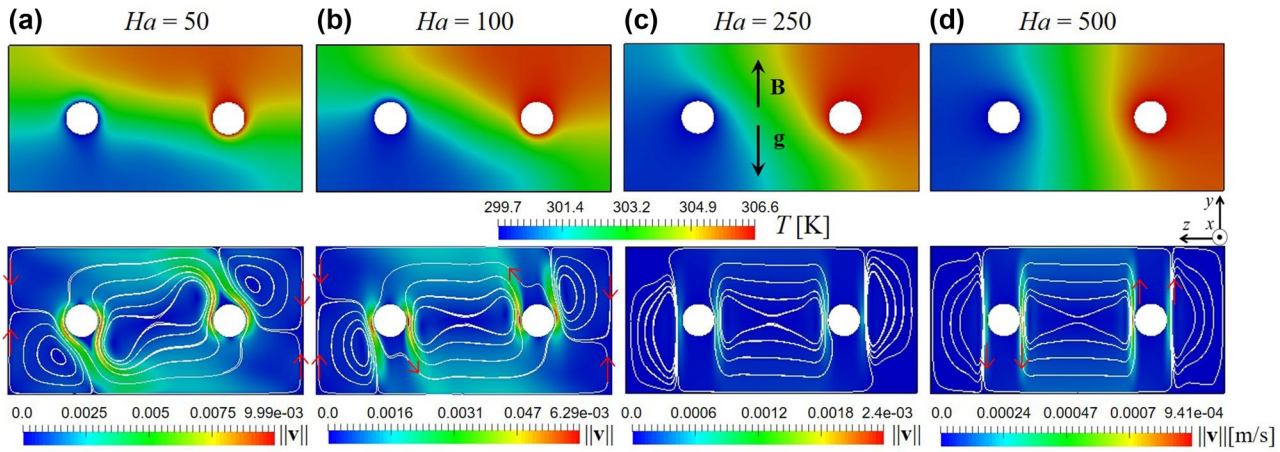

Fig. 7 Axially fully developed MHD convective flow at $Gr = 5 \cdot 10^6$ ($\Delta T = 3.475$ K) and four Hartmann numbers, $Ha = 50$ (**a**), 100 (**b**), 250 (**c**), 500 (**d**). Contours of temperature (top) and velocity magnitude (bottom) are plotted. White lines are velocity streamlines

As a result, for constant Gr, i.e. constant temperature difference between the pipes, Nu reduces significantly by increasing Ha.

4.3 Three dimensional flow

Three dimensional numerical simulations have been performed considering the real geometry of the test-section with finite axial length as used for experiments. The aim is on the one hand, to verify the possible limitations of the assumption of fully developed flow at a certain distance from the end-walls, as assumed for the 2D simulations, on the other hand, to provide a complete description of the phenomena involved by allowing current closure along end-walls. Moreover, numerical results complement experimental data and facilitate their interpretation. Dimensions of the geometry are given in Fig. 2. It is expected

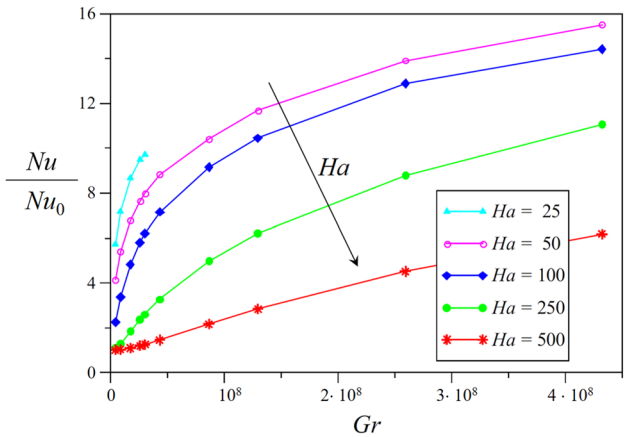

Fig. 8 Nusselt number Nu normalized by the one at $Gr = 0$, Nu_0, as a function of the Grashof number Gr for different Hartmann numbers Ha

that at the ends of the container in the parallel layers near $x = \pm 100$ mm, 3D MHD phenomena occur that produce significant electric potential gradients.

In the following we consider first the magneto-convective flow at a constant Hartmann number $Ha = 500$, where a temperature difference $\Delta T = 17.4$ K ($Gr = 2.5 \cdot 10^7$) is applied. In Fig. 9, the temperature distribution is plotted on the upper Hartmann wall, on the horizontal symmetry plane $y = 0$ (a), and on two yz planes at axial locations, x_{EW2} and x_P, corresponding to the end-wall of the box (EW2) at $x = 100$ mm and to the position of the tips of the thermocouples (CP) on the central temperature probe, respectively (b). In regions close to the end-walls the temperature varies along the axial direction. On the two yz end-walls a different temperature distribution is present compared to the one on the middle plane at $x = 0$ as a result of an increased convective heat transfer near these vertical planes. This is caused by higher velocities in the boundary layers that develop at walls parallel to the magnetic field, as displayed in Fig. 10, where 3D contours of the velocity distribution in the box are plotted on various planes. As already observed in the case of the 2D flow, internal layers are also present, which extend along the magnetic field direction, tangent to the pipes.

Contours of electric potential in the box are depicted in Fig. 11a. Significant potential differences arise near the end-walls of the geometry. Potential gradients drive currents in the adjacent boundary layers, which provide a closing path for the axial currents induced in the core flow.

Typical current streamlines are drawn in Fig. 11b. They are obtained by seeding tracers from points located in the parallel boundary layers both near the walls at $x = \pm 100$ mm and close to the side walls at $z = \pm 100$ mm. The 3D

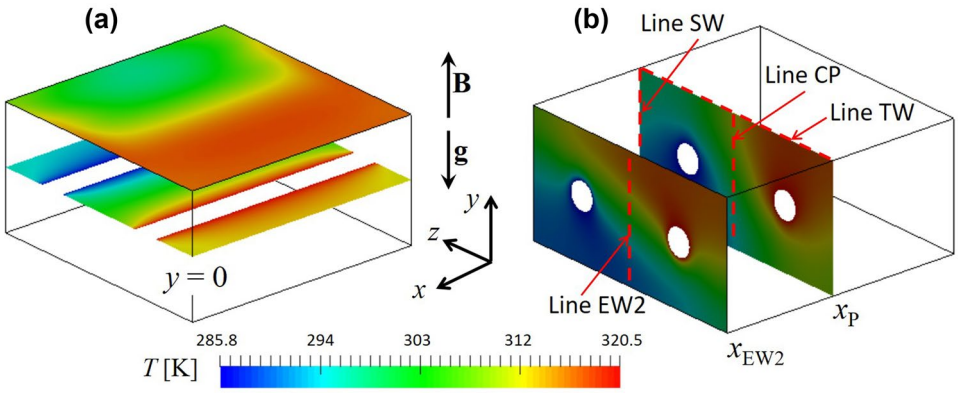

Fig. 9 Flow at $Ha = 500$, $Gr = 2.5 \cdot 10^7$. Temperature distributions on planes perpendicular to the magnetic field, at $y = 0$ (middle plane) and on the top Hartmann wall, TW (**a**), and on two yz planes (**b**). The coordinate x_{EW2} indicates the end-wall of the box at $x = 100$ mm and x_P the position of the tips of the thermocouples mounted on the central temperature probe, CP (Fig. 3). Along the dashed lines SW (side wall), EW2 (end-wall), CP (center probe) and TW (top wall) numerical and experimental data are compared later (see Fig. 4)

distribution of currents close to the end-walls of the test-section is clearly visible. Axial currents induced in the core flow close inside the side layers (green lines) and along the end-wall layers (red lines). Current streamlines displayed in blue originate from the middle core between the pipes. On the side walls at $z = \pm 100$ mm the topology of the electric current field is characterized by the presence of a saddle point at $x = 0$, as indicated by the green streamlines in the adjacent parallel boundary layer.

The influence of an increasing magnetic field on the flow at $Gr = 2.5 \cdot 10^7$ is shown in Figs. 12 and 13. In the former one, the flow at $Ha = 100$ is described. Contours of temperature on the symmetry plane at $x = 0$ (a) show that the isotherms are almost horizontal, as typical for a flow in which buoyancy forces dominate over the electromagnetic ones. A similar flow topology has been observed when assuming fully developed conditions in axial direction for weak magnetic fields, as shown e.g. in Fig. 5a. At the considered parameters, the flow features a large central convective cell, formed by the boundary layers at the pipe wall that detach and merge again behind the tube. Smaller recirculations with weaker convective motion are present between pipes and lateral side walls. The largest velocity is localized in internal and boundary layers, tangent to the

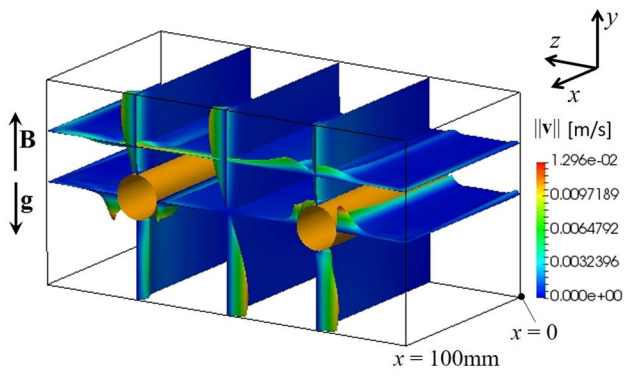

Fig. 10 Velocity distribution in the test-section for the flow at Ha =500 with an imposed temperature difference $\Delta T = 17.4$ K ($Gr = 2.5 \cdot 10^7$). The occurrence of internal layers tangent to the tubes can be seen in the figure, together with the increased velocity in the parallel boundary layers near the end-wall at $x = 100$ mm. Only half of the geometry is displayed in the figure

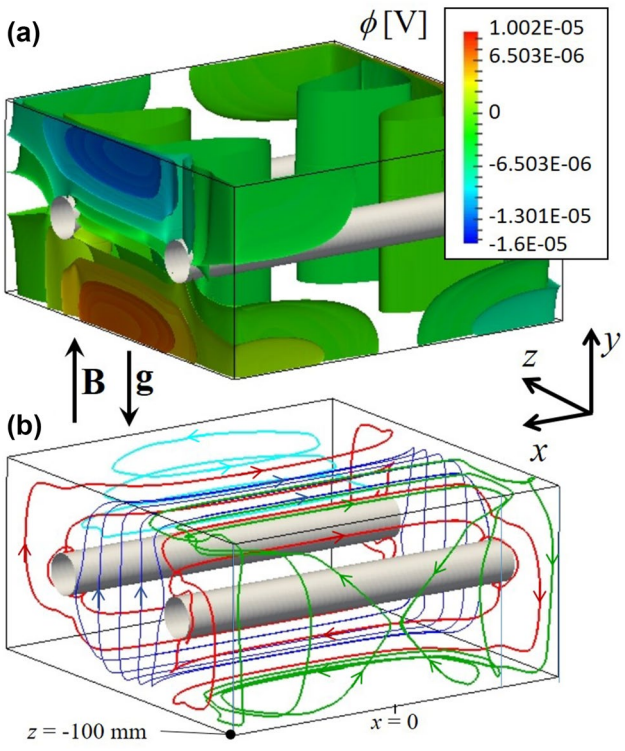

Fig. 11 Contours of electric potential in the test-section (**a**) and current streamlines (**b**) for the flow at $Ha = 500$ and $Gr = 2.5 \cdot 10^7$

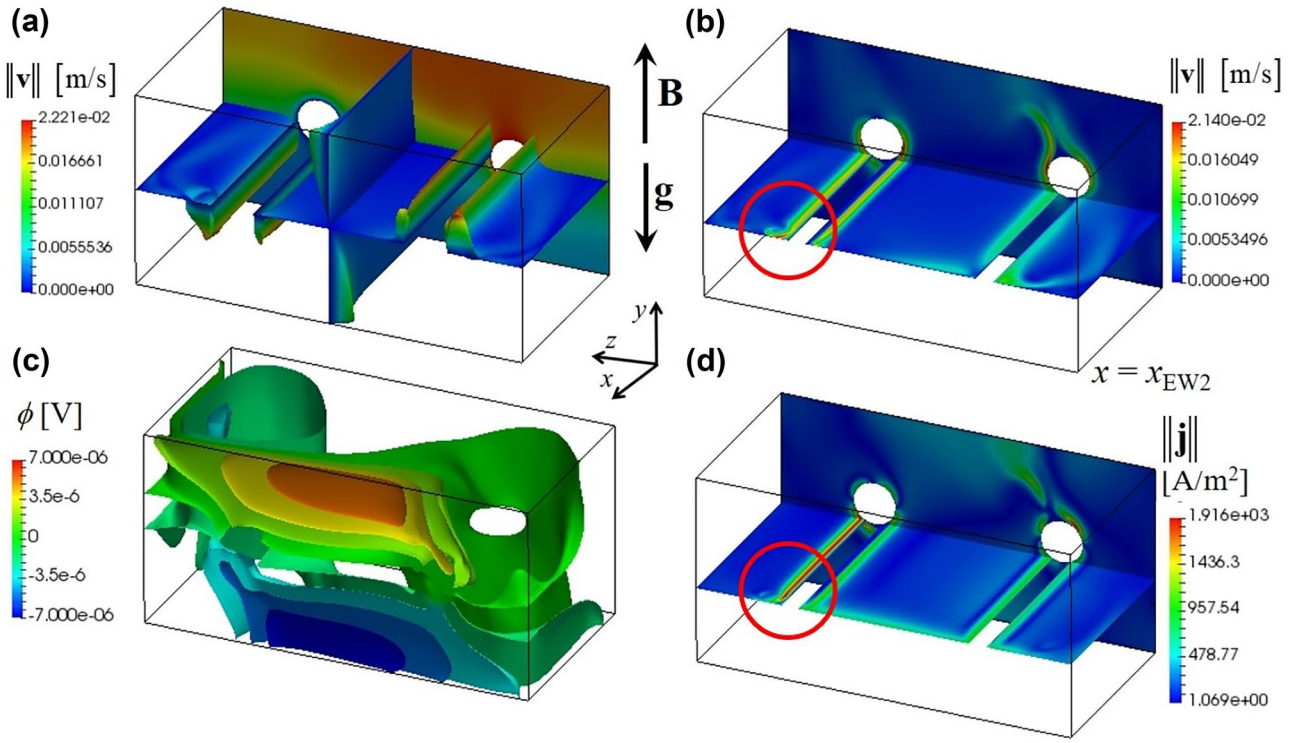

Fig. 12 MHD convective flows at $Gr = 2.5 \cdot 10^7$ and $Ha = 100$ displayed in half of the geometry. **a** 3D contours of velocity magnitude on the horizontal ($y = 0$) and vertical ($z = 0$) planes and contours of temperature on the plane $x = 0$. **b** Contours of velocity magnitude on the planes $y = -10$ mm and $x = 0$. **c** Iso-surfaces of electric potential. **d** Contours of current density on the planes $y = -10$ mm and $x = 0$

pipes and at the end-walls, respectively. This is visualized by velocity contours in Fig. 12(a, b). It can be observed that near the end-wall the intense convective motion leads to a detachment of the jet-like flow in the parallel layer and the formation of a swirling stream. This is also visible in the contours of current density on the plane at $y = -10$ mm in Fig. 12d, as marked by the red circle.

In Fig. 13 for the flows at $Gr = 2.5 \cdot 10^7$ and two Hartmann numbers, $Ha = 750$ (a) and $Ha = 2000$ (b), contours of velocity magnitude are plotted on horizontal and vertical middle planes of the box at $y = 0$ and $z = 0$, and contours of temperature on the plane $x = 0$ (top). On the bottom row of the figure, contours of electric potential are displayed. Results are shown only in one half of the box. For flows exposed to stronger magnetic fields, the convective heat transport is mainly confined in the parallel boundary layers along the end-walls of the container and in the fluid layers tangential to the pipes and aligned with the magnetic field. In the rest of the box the velocity is very small. By comparing temperature contours on the plane $x = 0$ for the smallest ($Ha = 100$) and the largest ($Ha = 2000$) Hartmann numbers considered in Figs. 12 and 13, it can be seen that the temperature distribution evolves in such a way that initially horizontal isotherms become vertical when electromagnetic forces grow. At $Ha = 2000$ the heat is transferred mainly by conduction. Contours of potential depicted in Fig. 13 (bottom) indicate that by increasing the intensity of the imposed magnetic field, potential gradients occur mostly in parallel layers at the end-walls.

4.4 Heat transfer and comparison between 2D and 3D simulations

The rate of heat transfer between pipes and liquid metal, expressed in nondimensional form by the Nusselt number (6) evaluated at the cylinder walls, is plotted in Fig. 14 as a function of the combined parameter Gr/Ha^2, which quantifies the relative importance of buoyancy and electromagnetic forces. Results obtained by assuming fully developed thermal and hydraulic conditions along x (2D simulations) and from 3D calculations considering the real geometry of the test-section are compared with the Nusselt numbers measured in the experimental campaign. Simulations have been performed for $4 \cdot 10^6 < Gr < 5 \cdot 10^7$ and $25 < Ha < 2000$.

When the Nusselt number increases it indicates that the convective heat transfer becomes more preponderant over the purely conductive one for which the Nusselt number was calculated to be $Nu_0 = 1.339$. This asymptotic value is indicated in the figure by the black dashed line. This conduction-dominated regime is found to occur for $Gr/Ha^2 \lesssim 15$ in 2D

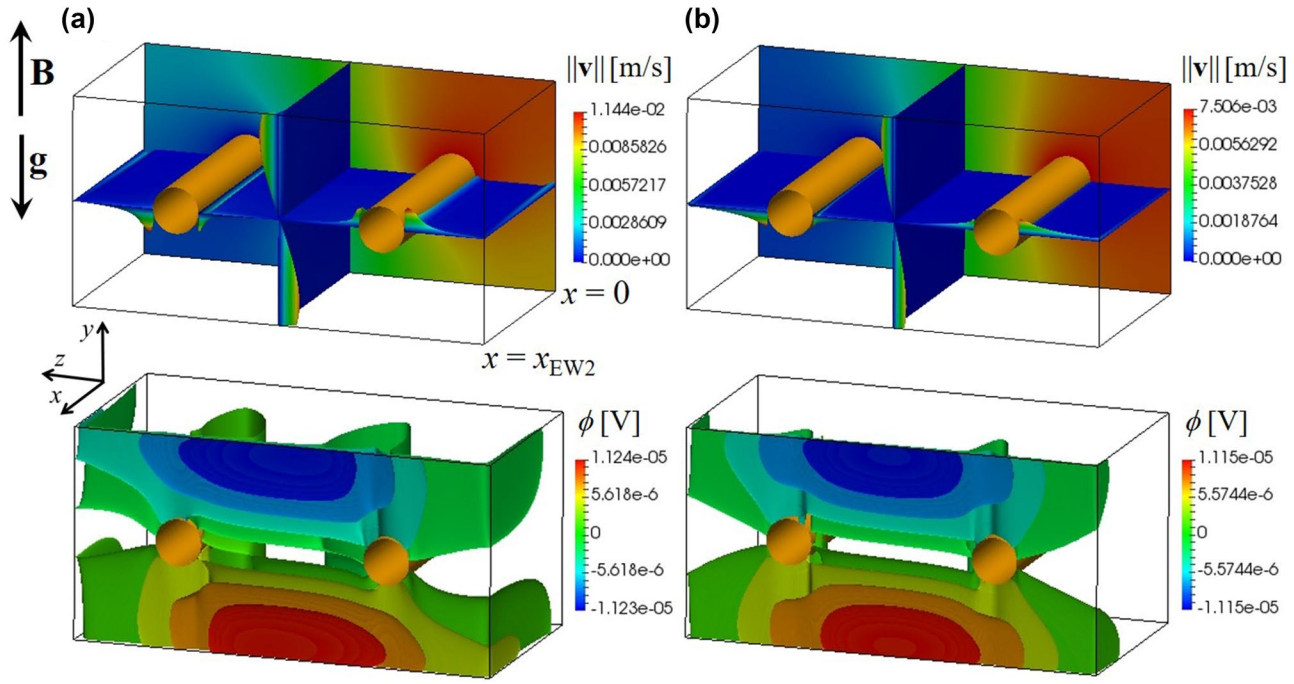

Fig. 13 MHD convective flows at $Gr = 2.5 \cdot 10^7$ and two Hartmann numbers, $Ha = 750$ (**a**), 2000 (**b**). Results are shown in half geometry. On the top, contours of velocity magnitude are plotted on horizontal ($y = 0$) and vertical ($z = 0$) middle planes and contours of temperature on the plane $x = 0$. On the bottom, contours of electric potential are visualized

simulations, while in 3D calculations for $Gr/Ha^2 \lesssim 2.5$. The larger threshold value observed when assuming fully developed flow conditions in 2D simulations is explained by the fact that a significant fraction of the total heat exchanged related to the convective motion near the end-walls is not taken into account by the 2D model. This is also the reason why 3D simulations predict higher Nusselt numbers than the 2D calculations.

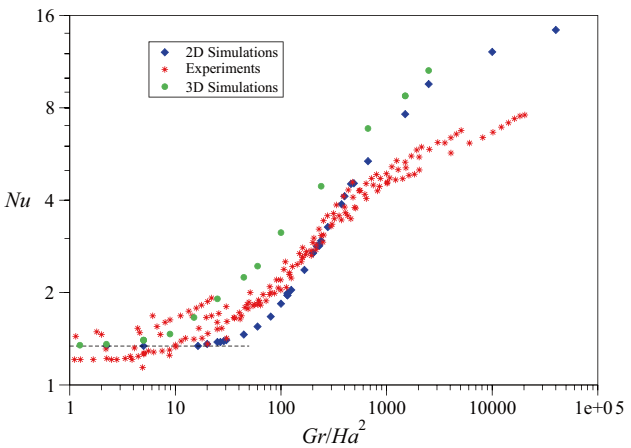

Fig. 14 Comparison of the Nusselt number measured in the experiments (stars) and the values calculated by means of 3D (circles) and 2D (rhombus) simulations. The black dashed line indicates the Nusselt number for $Gr = 0$, i.e. in case of pure conduction, $Nu_0 = 1.339$

In general there is a reasonable agreement between 3D simulations and experimental results. Both sets of data exhibit a similar scaling law, i.e. the heat transfer increases with analogous trend, in the range $20 < Gr/Ha^2 < 500$. An attempt to define a scaling law for the Nusselt number as a function of Gr/Ha^2 is presented in the companion paper about experiments [26]. Due to scattering in experimental data and possible heat losses to the ambient during the experiments that cannot be taken into account in the simulations, it is however difficult to find a general law that describes both measured and calculated values.

For $Gr/Ha^2 > 500$ the deviation between numerical and experimental results increases. One possible explanation could be that in this regime characterized by intense convective heat transfer (large Gr), the heat losses over walls in the experiments may be not negligible. It can also be observed that in the conductive regime, the Nusselt number predicted by numerical simulations and measured experimentally is of the same order of magnitude, with deviations smaller than 10%, which is within the experimental uncertainty.

In order to visualize graphically the convective heat transport, contours of $u_z \cdot (T - T_0)$ normalized by $u_0 \cdot \Delta T$ are plotted in Fig. 15 on the vertical middle plane of the box at $z = 0$ for $Gr = 2.5 \cdot 10^7$ and two Hartmann numbers, $Ha = 100$

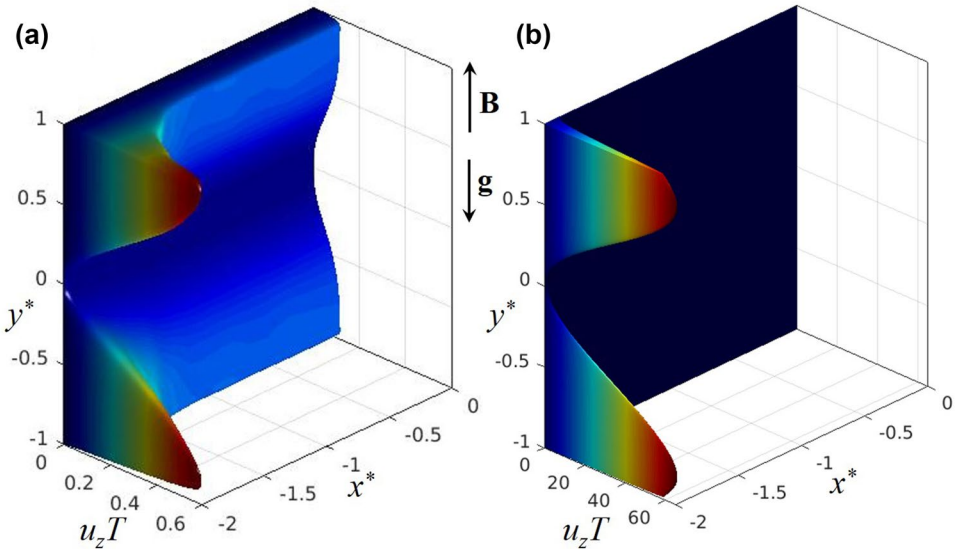

Fig. 15 Contours of the scaled convective heat $u_zT = u_z \cdot (T - T_0)/(u_0 \cdot \Delta T)$ on the plane $z = 0$ for flows at $Gr = 2.5 \cdot 10^7$ and two Hartmann numbers, $Ha = 100$ (**a**) and $Ha = 2000$ (**b**). The coordinates x and y have been normalized by $L = 50$ mm

(a) and $Ha = 2000$ (b). Results show clearly that the largest convective heat transport occurs in the parallel layer at the end-wall of the box, where a jet-like velocity profile is present (see Figs. 12a and 13b). As the strength of the magnetic filed increases from $B = 0.0504$ T, i.e. $Ha = 100$, to $B = 1.008$ T, i.e. $Ha = 2000$, the thickness $\delta_s \sim Ha^{-1/2}$ of the side layer decreases and the maximum intensity of the heat transported in the boundary region becomes two orders of magnitude larger.

In order to assess the predicting capabilities of 2D simulations, i.e. the validity of the assumption of fully developed thermal and hydraulic conditions, we compare the distribution of the transported convective heat as obtained by 3D and 2D simulations. In Fig. 16 the normalized convective heat u_zT is plotted for the flows at $Gr = 2.5 \cdot 10^7$ and two Hartmann numbers, $Ha = 500$ (a), 1000 (b), on the plane $z = 0$ both as 3D contours (left) and as profiles along the normalized vertical direction y^* at various axial positions (right). Results are compared with data from fully developed flows (2D). For sufficient distance from the end-wall, which depends on the characteristic flow parameters, the profile of the convective heat flux calculated by 3D simulations approaches the 2D distribution. For the flow at $Ha = 1000$ in the parallel layers at the end-walls the magnitude of u_zT is more than 30 times larger than the value near $x = 0$ and the one in the 2D solution.

It can be concluded that the assumption of fully developed thermal and hydraulic conditions leads to an accurate description of the flow only at sufficient distance from the end-walls. While reasonably predicting the main flow features at $x = 0$, such as the magnitude of convective heat transfer, the number of convective cells and the formation of internal tangent layers at large magnetic field, the 2D model underestimates considerably the transported convective heat in the entire geometry, since it does not take into account the occurrence of jet-like high velocity regions near the end-walls of the box, which provide a significant additional convective transport.

Another flow feature that cannot be described by 2D simulations is illustrated in Fig. 17, where the vertical velocity component v is plotted on the middle plane $y = 0$ along the z direction at an axial position close to the zy symmetry plane, as obtained both by 3D (solid lines) and 2D (dashed lines) simulations. The velocity profile between the pipes, which exhibits two counter flowing jets similarly to the flow in a differentially heated cavity [31], is well described also by assuming fully developed conditions. Instead, an additional vertical motion is predicted by 3D simulations in the boundary layers at the lateral walls at $z = \pm 100$ mm. This can be explained by the plot on the bottom left of the figure, which displays examples of velocity streamlines seeded in the parallel layers at the end-wall. The ascending and descending velocity that are not predicted by 2D simulations represent the closing path in the lateral parallel layers of those streamlines. As a result of the additional circulation near the side walls, a slightly lower temperature at the lateral wall is predicted by 3D simulations. For instance for $Ha = 500$ a difference of about 4 degrees is observed.

5 Comparison between simulations and experiments

Results from 3D numerical simulations are compared in the following with experimental data. The latter has been obtained in a campaign performed in the MEKKA facility at KIT as described briefly in Section 2. Details about the

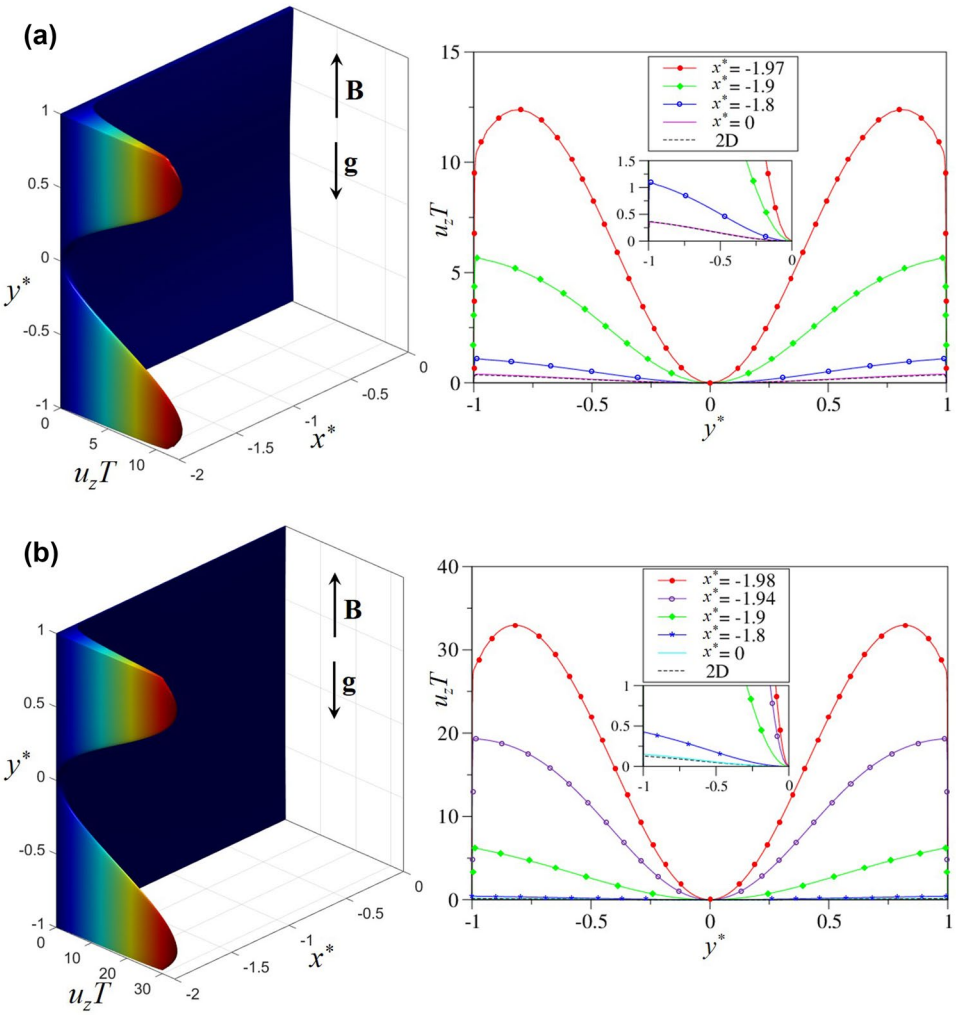

Fig. 16 Flows at $Gr = 2.5 \cdot 10^7$ and two Hartmann numbers, $Ha = 500$ (**a**) and $Ha = 1000$ (**b**). Contours on the plane $z = 0$ (left) and profiles along y^* (right) of the scaled convective heat $u_z \cdot (T - T_0)/(u_0 \cdot \Delta T)$. The coordinates have been normalized by $L = 50$ mm

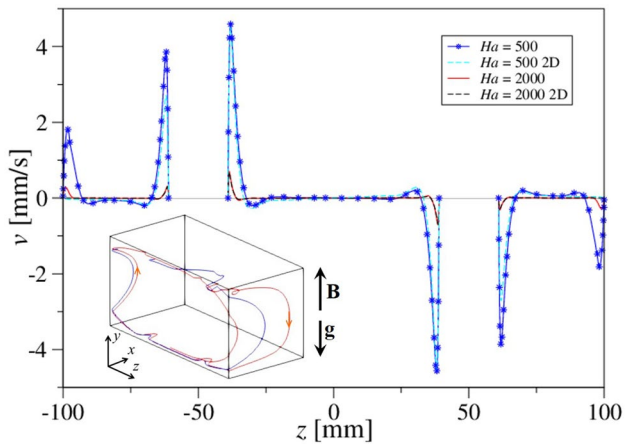

Fig. 17 Vertical velocity plotted along the z coordinate at $y = 0$, close to the symmetry plane for the flows at $Gr = 2.5 \cdot 10^7$ and two Hartmann numbers $Ha = 500$, 2000. Solid lines indicate results from 3D simulations and dashed lines those obtained under the assumption of fully established thermal and hydraulic conditions (2D). The picture on the bottom left displays examples of velocity streamlines showing the convective motion in the layers at the side walls of the box (end- and lateral walls)

experiments and more comprehensive sets of recorded data can be found in [26].

Temperature has been measured at many positions during the experiments (see Section 2 and Fig. 4). For recording the vertical distribution in the center of the test-section, a temperature probe with 11 thermocouples equidistantly distributed over the height of the box has been used, as shown in Fig. 3. In addition, the temperature on the walls of the test-section has been monitored at more than 50 positions to obtain an overview of the temperature distribution and to estimate the amount of transferred heat.

Experiments have been performed by keeping the mean temperature $\bar{T} = T_0 = (T_1 + T_2)/2$ constant and as close as possible to the ambient temperature in the magnet (30 °C), while adjusting the differential temperatures between the pipes to establish desired Grashof numbers Gr. Simulations have been carried out by following the same procedure. Some of the results are presented in nondimensional notation where the dimensionless temperature T^* is defined as

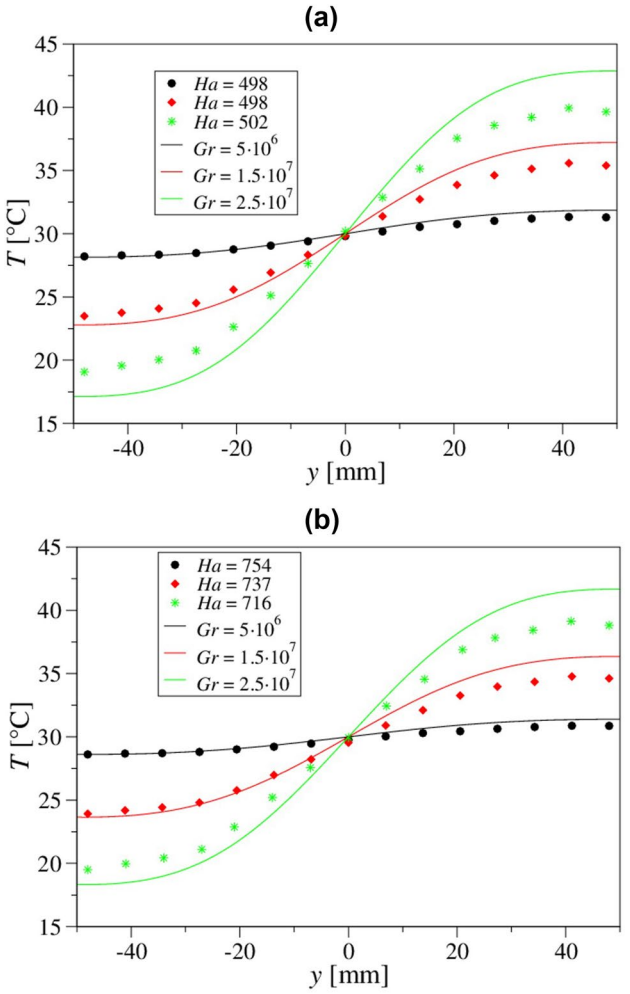

Fig. 18 Temperature profiles on the end-wall EW2 of the box ($x = 100$ mm, $z = 0$). The position of the sample lines are marked in Fig. 4. Comparison between numerical results (solid lines) and experimental data (symbols) for the flow at $Ha = 500$ (**a**) and $Ha = 750$ (**b**) and three Grashof numbers

$$T^* = \frac{T - \overline{T}}{\Delta T}.$$

In Fig. 18 numerical (solid lines) and experimental (symbols) results are compared on the end-wall of the test-section for the MHD flows at $Ha = 500$ (a) and $Ha = 750$ (b) and three Grashof numbers $Gr = 5 \cdot 10^6$ ($\Delta T = 3.475$ K), $1.5 \cdot 10^7$ ($\Delta T = 10.424$ K), $2.5 \cdot 10^7$ ($\Delta T = 17.4$ K). A good agreement is observed for all sets of data. When the Grashof number is small, numerical results and experiments fit better together, since all temperatures come closer to the ambient value and parasitic heat exchange with the environment reduces in the experiments.

In Fig. 19 numerical and experimental data along the central probe (CP) are compared for different Hartmann numbers

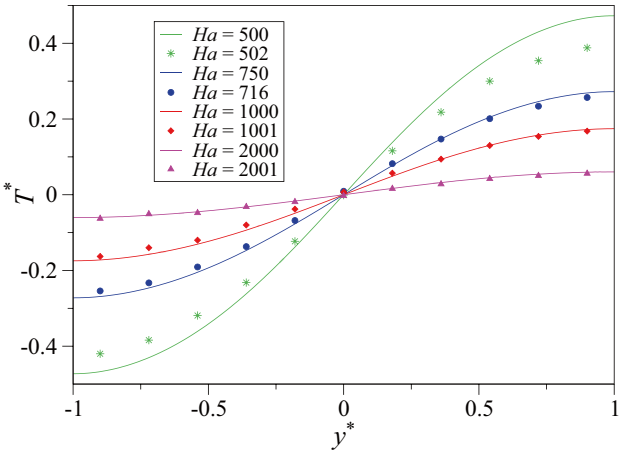

Fig. 19 Dimensionless temperature profiles at the central probe (CP) near the middle of the test-section. Comparison between numerical results (solid lines) and experimental data (symbols) for the flow at $Gr = 2.5 \cdot 10^7$ and different Hartmann numbers. The y coordinate has been normalized by $L = 50$ mm

and $Gr = 2.5 \cdot 10^7$. A good agreement between 3D simulations and experiments is also found here for nearly all investigated Hartmann numbers. Some deviations occur for the moderate Hartmann number $Ha = 500$ (green symbols and line), for which the largest temperature difference between top and bottom wall is observed. As already mentioned, unexpected parasitic heat losses in the experiments across the finite thermal insulation could be the reason for those discrepancies. Experimental data used for the comparison in Fig. 19 have been plotted by defining a reference temperature such that $T^*_{y^*=0} = 0$.

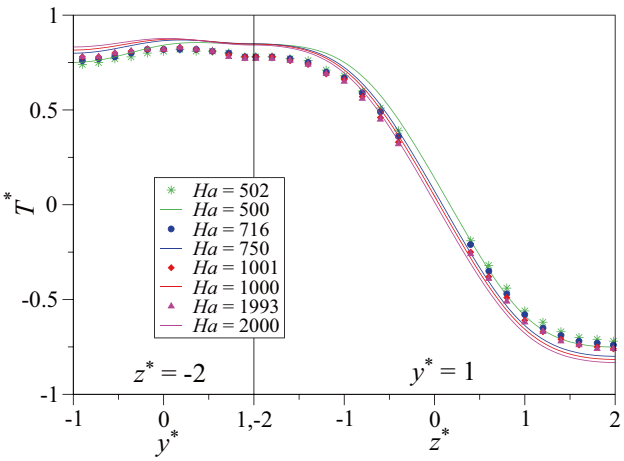

Fig. 20 Dimensionless temperature profiles on the side wall (SW) for $-1 \leqslant y^* \leqslant 1$ and on the top wall (TW) for $-2 \leqslant z^* \leqslant 2$. Comparison between numerical results (solid lines) and experimental data (symbols) for the flow at $Gr = 5 \cdot 10^6$ and different Hartmann numbers. The y and z coordinates have been normalized by $L = 50$ mm

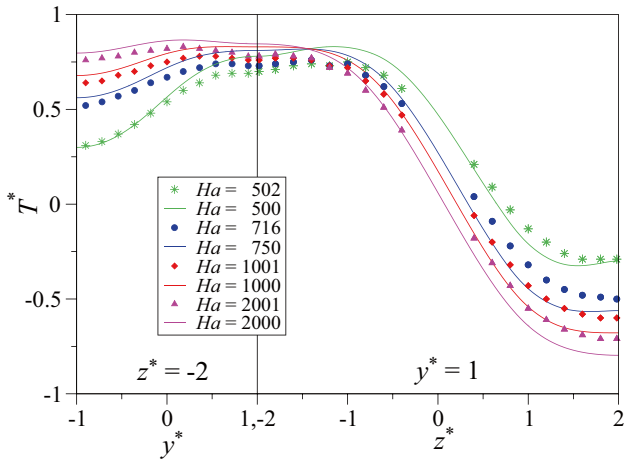

Fig. 21 Dimensionless temperature profiles on the side wall (SW) for $-1 \leqslant y^* \leqslant 1$ and on the top wall (TW) for $-2 \leqslant z^* \leqslant 2$. Comparison between numerical (solid lines) and experimental (symbols) data for the flow at $Gr = 2.5 \cdot 10^7$ and different Hartmann numbers. The y and z coordinates have been normalized by $L = 50$ mm

In Figs. 20 and 21 profiles of normalized time-averaged temperature are plotted along the side wall (SW) for $-1 \leqslant y^* \leqslant 1$ and on the top wall (TW) for $-2 \leqslant z^* \leqslant 2$ for the flows at four Hartmann numbers, and two Grashof numbers $Gr = 5 \cdot 10^6$ and $Gr = 2.5 \cdot 10^7$, respectively. The y and z coordinates have been normalized by $L = 50$ mm.

When the temperature difference between the pipes is moderate, e.g. for $Gr = 5 \cdot 10^6$, the convective motion is very weak in particular if the magnetic field is intense (large Ha). As a consequence, the temperature field at $x = x_P$, close to the middle plane, is similar for all the Hartmann numbers considered in Fig. 20 and it is characterized by isotherms that tend to align with the y - direction, as typical for pure conduction. This is shown by the quite uniform temperature distribution on the side wall ($-1 \leqslant y^* \leqslant 1$). As the Grashof number increases, the curves depart from each other, since the stronger convection affects the temperature distribution, as depicted in Fig. 21 for the flows at $Gr = 2.5 \cdot 10^7$ and four Hartmann numbers. At $Ha = 2000$, the temperature profiles on SW and TW are very similar for both Grashof numbers, since electromagnetic forces dominate and damp the convective motion.

6 Conclusions

In order to investigate fundamental aspects of magneto-convective flows relevant for WCLL blankets, numerical simulations have been performed for a model problem, where two isothermal parallel cylinders immersed in a box filled with liquid metal are kept at differential temperature $T_2 - T_1$. A constant magnetic field is imposed perpendicular to the axes of the cylinders and parallel to gravity. The selected geometrical configuration corresponds to the one used for an experimental campaign carried out in the MEKKA laboratory at KIT [26]. Resulting flow patterns and heat transfer in the container are investigated depending on the driving buoyant force given in terms of the Grashof number Gr and the braking Lorentz force expressed by the Hartmann number Ha. Simulations have been performed for parameters in the range $4 \cdot 10^6 < Gr < 5 \cdot 10^7$ and $50 < Ha < 2000$, at a Prandtl number $Pr = 0.029$.

Numerical results show that electromagnetic forces significantly slow down the convective motion that results from the non-uniform thermal conditions caused by the imposed temperature difference between the cylinders. Under intense magnetic fields, the flow features a central, almost square convective cell bounded by the fluid layers, which develop parallel to the magnetic field and tangent to the pipes. In the rest of the container the fluid velocity is very small. Eventually, when Ha becomes large enough, the problem tends to an asymptotic solution where the heat transfer is completely dominated by conduction and the temperature field is characterized by vertical isotherms. On the other hand, when buoyancy forces become predominant, a thermal stratification with horizontal isotherms develops in the box such that the warm liquid metal is localized near the top wall and colder fluid on the bottom. This is due to an intense convective heat transport that promotes a more stable density stratification.

The intensity of convective heat transfer has been quantified by the Nusselt number, Nu. The competition between buoyancy forces promoting the convection and electromagnetic forces suppressing the buoyant flow becomes evident by looking at the variation of Nu as a function of Gr and Ha. The Nusselt number has been calculated by performing both 2D and 3D numerical simulations and results have been compared with experimental data. The outcome clearly shows that the increased convective heat transfer near the end-walls of the box contributes significantly to the total transferred heat. Therefore, a pure 2D analysis cannot be used to accurately quantify the heat exchanged between pipes and fluid in a geometry of finite axial extension. While both 2D and 3D models describe well the main flow features, such as velocity and temperature distribution and heat flux, in the middle of the test-section, the increased convective heat transfer in the boundary layers at the end-walls can be predicted only by full 3D analyses.

A good agreement has been found between 3D numerical results and experimental data when comparing temperature profiles at different locations on the surface of the box and inside the fluid. For large Gr some deviation is observed probably due to the increased heat losses in the experiments.

It should be mentioned that the heat transfer is affected not only by the characteristic flow parameters but also by the orientation of the magnetic field with respect to the

cavity walls [32, 33]. In the present work, we considered a magnetic field with a single component perpendicular to the cylinder axes, according to the **B** configuration present in the experiments. Since the magnetic field in a fusion blanket is more complex, the effects of magnetic field orientation on the analyzed flow should be investigated as well.

It has been also observed that the flow in the parallel layers at the end-walls may exhibit instabilities even if the flow in the middle of the box is stable. Depending on the flow conditions, dynamic patterns appear triggered by increased buoyancy effects. A complementary analysis of time-dependent flows is currently being performed and those results will be presented in a separate paper.

Acknowledgements This work has been carried out within the framework of the EUROfusion Consortium and has received funding from the Euratom research and training programme 2014-2018 and 2019-2020 under grant agreement No 633053. The views and opinions expressed herein do not necessarily reflect those of the European Commission. This work was carried out (partially) using supercomputer resources provided under the EU-JA Broader Approach collaboration in the Computational Simulation Centre of International Fusion Energy Research Centre (IFERC-CSC).

Author contributions Conceptualization, writing - original draft preparation, editing and review, numerical simulations, C. Mistrangelo; writing - review and editing, L. Bühler; experiments, data acquisition, H-J. Brinkmann; experiments, data acquisition and analysis, C. Courtessole; numerical pre-processing, V. Klüber; numerical pre-processing, C. Koehly. All authors have agreed to the published version of the manuscript.

Funding Open Access funding enabled and organized by Projekt DEAL.

Declarations

Conflict of interest The authors state that there is no conflict of interest and have no competing interests to declare that are relevant to the content of this article.

References

1. Federici G, Boccaccini L, Cismondi F, Gasparotto M, Poitevin Y, Ricapito I (2019) An overview of the EU breeding blanket design strategy as an integral part of the DEMO design effort. Fusion Eng Des 141:30–42. https://doi.org/10.1016/j.fusengdes.2019.01.141
2. Del Nevo A, Arena P, Caruso G, Chiovaro P, Maio PD, Eboli M, Edemetti F, Forgione N, Forte R, Froio A, Giannetti F, Gironimo GD, Jiang K, Liu S, Moro F, Mozzillo R, Savoldi L, Tarallo A, Tarantino M, Tassone A, Utili M, Villari R, Zanino R, Martelli E (2019) Recent progress in developing a feasible and integrated conceptual design of the WCLL BB in EUROfusion project. Fusion Eng Des 146:1805–1809. https://doi.org/10.1016/j.fusengdes.2019.03.040
3. Gardner RA, Lykoudis PS (1971) Magneto-fluid-mechanic pipe flow in a transverse magnetic field part 2. Heat transfer. J Fluid Mech 48:129–141
4. Al-Khawaja MJ, Agarwal RK, Gardner RA (1999) Numerical study of magneto-fluid-mechanic combined free-and-forced convection heat transfer. Int J Heat Mass Transf 42:467–475
5. Zhang X, Zikanov O (2014) Mixed convection in a horizontal duct with bottom heating and strong transverse magnetic field. J Fluid Mech 757:33–56. https://doi.org/10.1017/jfm.2014.473
6. Sahu S, Courtessole C, Ranjan A, Bhattacharyay R, Sketchley T, Smolentsev S (2020) Thermal convection studies in liquid metal flow inside a horizontal duct under the influence of transverse magnetic field. Phys Fluids 32:067107. https://doi.org/10.1063/5.0006260
7. Ben Hadid H, Henry D (1996) Numerical simulation of convective three-dimensional flows in a horizontal cylinder under the action of a constant magnetic field. J Cryst Growth 166:436–445
8. Tagawa T, Ozoe H (1998) The natural convection of liquid metal in a cubical enclosure with various electroconductivities of the wall under the magnetic field. Int J Heat Mass Transf 41:1917–1928
9. Chen L, Liu B-Q, Ni M-J (2018) Study of natural convection in a heated cavity with magnetic fields normal to the main circulation. Int J Heat Mass Transf 127:267–277. https://doi.org/10.1016/j.ijheatmasstransfer.2018.06.019
10. Burr U, Müller U (2001) Rayleigh-Bénard convection in liquid metal layers under the influence of a vertical magnetic field. Phys Fluids 13:3247–3257
11. Zürner T, Schindler F, Vogt T, Eckert S, Schumacher J (2019) Combined measurement of velocity and temperature in liquid metal convection. J Fluid Mech 876:1108–1128. https://doi.org/10.1017/jfm.2019.556
12. Zikanov O, Belyaev I, Listratov Y, Frick P, Razuvanov N, Sviridov V (2021) Mixed convection in pipe and duct flows with strong magnetic fields. Appl Mech Rev 73:010801–1–35. https://doi.org/10.1115/1.4049833
13. Davidson PA (1999) Magnetohydrodynamics in materials processing. Annu Rev Fluid Mech 31:273–300
14. Oreper GM, Szekely J (1983) The effect of an externally imposed magnetic field on buoyancy driven flow in a rectangular cavity. J Cryst Growth 64:505–515. https://doi.org/10.1016/0022-0248(83)90335-4
15. Ozoe H, Szmyd JS, Tagawa T (2007) Magnetic Fields in Semiconductor Crystal Growth, Springer Netherlands, Dordrecht, pp. 375–390
16. House JM, Beckermann C, Smith TF (1990) Effect of a centered conducting body on natural convection heat transfer in an enclosure. Numerical Heat Transfer, Part A: Applications 18:213–225. https://doi.org/10.1080/10407789008944791
17. Costa V (2012) Natural convection in partially divided square enclosures: Effects of thermal boundary conditions and thermal conductivity of the partitions. Int J Heat Mass Transf 55:7812–7822. https://doi.org/10.1016/j.ijheatmasstransfer.2012.08.004
18. Son JH, Park IS (2017) Numerical study of MHD natural convection in a rectangular enclosure with an insulated block. Numerical Heat Transfer, Part A: Applications 71:1004–1022. https://doi.org/10.1080/10407782.2017.1330090
19. Bühler L, Mistrangelo C (2017) MHD flow and heat transfer in model geometries for WCLL blankets. Fusion Eng Des 122:919–923. https://doi.org/10.1016/j.fusengdes.2017.01.014
20. Mistrangelo C, Bühler L, Koehly C (2019) Considerations on magneto-convective flows in model geometries relevant for fusion applications.

In: Proceedings of the 11th International PAMIR Conference - Fundamental and Applied MHD, July 01 - 05, 2019, Reims, France, pp. 7–11
21. Yan Y, Ying A, Abdou M (2020) Numerical study of magneto-convection flows in a complex prototypical liquid-metal fusion blanket geometry. Fusion Eng Des 159:111688. https://doi.org/10.1016/j.fusengdes.2020.111688
22. Tassone A, Caruso G, Giannetti F, Nevo AD (2019) MHD mixed convection flow in the WCLL: heat transfer analysis and cooling system optimization. Fusion Eng Des 146
23. Davidson PA (2001) An Introduction to Magnetohydrodynamics, Cambridge University Press
24. Koehly C, Bühler L, Mistrangelo C (2019) Design of a test section to analyze magneto-convection effects in WCLL blankets. Fusion Sci Technol 75:1010–1015. https://doi.org/10.1080/15361055.2019.1607705
25. Barleon L, Mack KJ, Stieglitz R (1996) The MEKKA-facility a flexible tool to investigate MHD-flow phenomena, Technical Report FZKA 5821, Forschungszentrum Karlsruhe
26. Courtessole C, Brinkmann HJ, Bühler L (2023) Experimental investigation on magneto-convective flows around two differentially heated cylinders, Heat and Mass Transfer. Under review.
27. Plevachuk Y, Sklyarchuk V, Eckert S, Gerbeth G, Novakovic R (2014) Thermophysical properties of the liquid ga-in-sn eutectic alloy. J Chem Eng Data 59:757–763. https://doi.org/10.1021/je400882q, arXiv:http://dx.doi.org/10.1021/je400882q
28. Ni M-J, Munipalli R, Morley NB, Huang P, Abdou MA (2007a) A current density conservative scheme for incompressible MHD flows at a low magnetic Reynolds number. Part I: On a rectangular collocated grid system. Journal of Computational Physics 227:174–204
29. Ni M-J, Munipalli R, Huang P, Morley NB, Abdou MA (2007b) A current density conservative scheme for incompressible MHD flows at a low magnetic Reynolds number. Part II: On an arbitrary collocated mesh. J Comput Phys 227:205–228
30. Smolentsev S, Badia S, Bhattacharyay R, Bühler L, Chen L, Huang Q, Jin H-G, Krasnov D, Lee D-W, Mas de les Valls E, Mistrangelo C, Munipalli R, Ni MJ, Pashkevich D, Patel A, Pulugundla G, Satyamurthy P, Snegirev A, Sviridov V, Swain P, Zhou T, Zikanov O (2015) An approach to verification and validation of MHD codes for fusion applications. Fusion Eng Des 100:65–72. https://doi.org/10.1016/j.fusengdes.2014.04.049
31. Rudraiah N, Barron RM, Venkatachalappa M, Subbaraya CK (1995) Effect of a magnetic field on free convection in a rectangular enclosure. Int J Eng Sci 33:1075–1084. https://doi.org/10.1016/0020-7225(94)00120-9
32. Ozoe H, Okada K (1989) The effect of the direction of the external magnetic field on three-dimensional natural convection in a cubical enclosure. Int J Heat Mass Transf 32:1939–1954
33. Yu P, Qiu J, Qin Q, Tian ZF (2013) Numerical investigation of natural convection in a rectangular cavity under different directions of uniform magnetic field. Int J Heat Mass Transf 67:1131–1144. https://doi.org/10.1016/j.ijheatmasstransfer.2013.08.087